Computational Fluid Dynamics JOURNAL vol.5 no.4 January 1997 (pp.471–486)

NUMERICAL ANALYSIS OF DEVELOPING TURBULENT STRUCTURE IN A CIRCULAR-TO-RECTANGULAR TRANSITION DUCT

Hitoshi SUGIYAMA † Mitsunobu AKIYAMA † Daisuke HITOMI †

Abstract

Numerical analysis is applied to three-dimensional turbulent flow in a circular-to-rectangular transition duct, which is characterized by the streamwise curvature of streamlines and the vorticity embedded in the boundary layer. In the calculation, an algebraic Reynolds stress model together with a boundary-fitted coordinate system is used to simulate precisely the anisotropic turbulent flows. The calculated results are compared with the experimental results by Davis and Gessner (AIAA J., vol.30 pp.367–375). The physical quantities compared include the static pressure, the three components of the mean velocity vector, the six components of the Reynolds stress tensor and the invariant of the anisotropic tensor. The present method predicts correctly the secondary flow pattern which develops into a discrete vortex pair along the duct sidewalls. This secondary flow arises as a result of lateral skewing of the near-wall flow induced by the transverse pressure gradients. This vortex pair significantly distorts both of the mean flow and turbulence fields. It is found that the present method using the algebraic Reynolds stress model can provide reasonable flow simulation.

1. INTRODUCTION

The duct which has a varying cross sectional shape along streamwise direction refers here as the transition duct. Such ducts are commonly used in the systems of ventilation, aircraft propulsion, wind tunnel, diffusers of hydroelectric turbines, *etc.* Those of current interests are the circular-to-rectangular (CR) duct, one of which, engine exhaust nozzle of rectangular cross section, has been under development in order to improve aircraft performance. Another is hydraulic CR transition duct with a 90 degree bend, which is used to diffuse the water exiting from the vertical turbine runner.

Mayer [1] firstly investigated experimentally rectangular-to-circular (and vice versa) transition duct flows in 1939, and gave streamwise static pressure distributions and contours of total pressure and the three-dimensional velocity. Taylor *et al.* [2] measured flows through a duct which transformed from a 40 mm square cross section to a 40 mm diameter circular cross section along 80 mm tube length, which results 21.5 % reduction of cross-sectional area. This decrease is derived from keeping the hydraulic diameter constant. Laser-Doppler velocimetry

Received on July 19, 1996.
† Dept. of Mechanical Systems Engineering, Utsunomiya University;
2753 Ishii-cho, Utsunomiya, 321 Japan

(LDV) measurements of streamwise and transverse velocity along the duct were carried out at a Reynolds number of 35,350.

Patrick and McCormick [3] were the first to measure the turbulent structure within a CR transition duct by LDV and total pressure measurements at the inlet and outlet stations of two different ducts at a Reynolds number of 420,000. The first duct has an aspect ratio of three, a length-to-diameter ratio of one, and constant cross-sectional area through the duct. The second duct has an aspect ratio of six and a length-to-diameter ratio of three. The local cross sectional area ratio increases from unity at the inlet to a maximum of 1.10 at the midpoint before decreasing back to unity at the duct exit. They concluded that the secondary flows can play an important role in the fluid dynamics of transition ducts and needs to be addressed in computational analysis. Adding to this, they reported that the strength of the secondary flows depends on both the aspect ratio and relative axial duct length.

Miau *et al.* [4] experimentally investigated three CR ducts with length-to-diameter ratios of 1.08, 0.92 and 0.54 under low subsonic conditions. The aspect ratio was equal to two and cross-sectional area was constant for all three ducts. They showed that the generation of streamwise vorticity is due primary to transverse pressure gradients induced by geometrical deformation. Reichert *et al.* [5] examined CR transition duct flows with and without inlet swirl in order to understand the effect of inlet swirl on the transition duct flow field and to provide detailed duct flow data for comparison with numerical code prediction.

From the review of literature revealed that there is only a small experimental database for flow through CR transition duct, Davis and Gessner [6] measured the turbulent structure contained the six Reynolds stress components in detail. Their experimental results are intended not only to provide insight into the physics of the flow, but also to serve as a basis for testing turbulent models applicable to this type of flow situation.

In numerical analysis, Lien and Leschziner [7] presented numerical results of CR transition duct compared with the experimental data measured by Davis and Gessner [6] by using high-Reynolds and low-Reynolds k-ϵ turbulent model. Although they compared the calculated results of transverse velocity with the experimental data, the discrepancy between both results is observed as the flow develops downstream. Vu and Shyy [8] performed three-dimensional turbulent viscous flow analysis for hydraulic turbine elbow draft tubes by solving Reynolds averaged Navier-Stokes equations closed with a two-equation turbulence model. They reported that pressure recovery factor and flow behavior in the draft tube with a wide range of swirling flows at the inlet agree well with experimental data. Although there are a few reports of numerical analysis for CR transition duct, no satisfactory analysis, to our knowledge, exists which would predict the all Reynolds stress components.

Judging from the review of literature mentioned the above, the main object is to predict the turbulent structure of CR transition duct by using algebraic Reynolds stress model. The boundary-fitted coordinate system is adopted in this study as the method of coordinate transformation. The calculated results are compared with the experimental data measured by Davis and Gessner [6] in order to examine the validity of the present method and to provide insight into the physics of CR transition duct.

2. TECHNIQUE OF ANALYSIS

2.1 Subject of Numerical Analysis

In numerical analysis, the experimental data measured in detail by Davis and Gessner [6] was selected as a subject of calculation. Figure 1 shows a schematic diagram of the experimental apparatus and the coordinate system set in CR transition duct. The origin of the coordinate system lies midway between $X_1/R = -1.0$ and 1.0, where R is pipe radius. The CR transition duct has an exit aspect ratio of 3.0 and a transition length of 4.5 inlet diameters(inlet diameter D=20.42 cm) which changes in cross-sectional shape occur. The cross-sectional configuration is defined by the equation of a superellipse, namely:

$$\left(\frac{X_2}{a}\right)^{\eta} + \left(\frac{X_3}{b}\right)^{\eta} = 1 \tag{1}$$

where a and b are the semi-major and semi-minor axes of the superellipse, respectively and a, b and η are functions of the streamwise coordinate X_1 which are described by Davis [9] in detail. The cross-sectional area begins to increase at the start of transition to a maximum of 15 % above the inlet cross-sectional area, occurring approximately at the mid-point of transition. From there the area smoothly decreases until the end of transition where the cross-sectional area is equal to the inlet cross-sectional area. From the 20:1 contraction, the flow enters a 20.42 cm diameter straight pipe, 184 cm in length. Downstream of the transition duct, the flow enters a rectangular duct of 89 cm in length.

In the experiment, Reynolds number evaluated on a axial bulk velocity U_b and pipe diameter D was kept at $R_e = 3.9 \times 10^5$. Mean flow and turbulence data were obtained by means of pressure probe and hot-wire instrumentation. The turbulence measurement is carried out especially for the cross sections of $X_1/R = 4.0$ and 8.0.

2.2 Algebraic Reynolds Stress Model

The anisotropy nature of the turbulence was expressed precisely by the Reynolds stress equations. Nevertheless, an exact analysis of these equations is not yet available so that some modeling effort was required. The set of differential equations governing the transport of the Reynolds stresses is derived from the Navier-Stokes equation as follows:

$$\begin{aligned}\frac{D\overline{u_iu_j}}{Dt} = &- \left(\overline{u_iu_k}\frac{\partial U_j}{\partial x_k} + \overline{u_ju_k}\frac{\partial U_i}{\partial x_k}\right) + \overline{\frac{p}{\rho}\left(\frac{\partial u_i}{\partial x_j} + \frac{\partial u_j}{\partial x_i}\right)} \\ &- \frac{\partial}{\partial x_k}\left[\overline{u_iu_ju_k} - \nu\frac{\partial \overline{u_iu_j}}{\partial x_k} + \overline{\frac{p}{\rho}(\delta_{jk}u_i + \delta_{ik}u_j)}\right] - 2\nu\overline{\frac{\partial u_i}{\partial x_k}\frac{\partial u_j}{\partial x_k}}\end{aligned} \tag{2}$$

As for the modeling of the convective term and of the diffusion term,the approximation by Rodi [10] was employed. By Rodi's approximation, these terms expressed in a differential form for Reynolds stress component can be transformed into the algebraic equation. In the Reynolds stress model equation, a particularly problematic task is the modeling of the pressure-strain correlation term which is also defined redistribution term. The pressure-strain term is shown in Table 1 and the constants used in this analysis are summarized in Table 2. In the modeling of $\pi_{ij,2}$, we made use of the forth-order tensor presented by Launder, Reece and Rodi [11].

Moreover, kinematic constraints presented by Gessner and Eppich [12] are adopted in this research. Authors [13] described the derivation of pressure-strain and its constants in detail. In Table 1, $f(L/X_w)$ is a function of the dimensionless wall distance. It expresses the influence of the wall and takes the value 1 in its vicinity, approaching 0 in with the increasing distance of it. X_w expresses the distance from the wall and L defined length scale of turbulence.

Table 1: Modeling of the pressure-strain correlation term

$\pi_{ij,1} + \pi_{ji,1}$	$-C_1\frac{\varepsilon}{k}\left(\overline{u_iu_j} - \frac{2}{3}k\delta_{ij}\right)$
$\pi_{ij,2} + \pi_{ji,2}$	$-\frac{C_2+8}{11}\left(P_{ij} - \frac{2}{3}P_k\delta_{ij}\right) + \zeta k\left(\frac{\partial U_i}{\partial x_j} + \frac{\partial U_j}{\partial x_i}\right)$ $-\frac{8C_2-2}{11}\left(D_{ij} - \frac{2}{3}P_k\delta_{ij}\right)$
$[\pi_{ij} + \pi_{ji}]_w$	$C_1 = C_1^* + C_1' f\left(\frac{L}{X_w}\right)$ $C_2 = C_2^* + C_2' f\left(\frac{L}{X_w}\right)$ $\zeta = \zeta^* + \zeta' f\left(\frac{L}{X_w}\right)$
$P_{ij} = -\overline{u_iu_k}\frac{\partial U_j}{\partial x_k} - \overline{u_ju_k}\frac{\partial U_i}{\partial x_k}$ $D_{ij} = -\overline{u_iu_k}\frac{\partial U_k}{\partial x_j} - \overline{u_ju_k}\frac{\partial U_k}{\partial x_i}$ $P_k = -\overline{u_ku_l}\frac{\partial U_k}{\partial x_l}$ $f\left(\frac{L}{X_w}\right) = \frac{C_\mu^{\frac{3}{4}}k^{\frac{3}{2}}}{\kappa}\frac{1}{\varepsilon}\frac{1}{X_w}$	

Table 2: Constants in the pressure-strain correlation term

C_1^*	C_2^*	ζ^*	C_1'	C_2'	ζ'
1.4	0.44	-0.16	-0.35	0.12	-0.1

In this research, boundary-fitted coordinate system (BFC) was adopted as the coordinate transformation. The transformation of the governing equations to the calculation level is accomplished according to following mathematical definitions:

$$\frac{\partial}{\partial X_i} = \frac{\partial \xi}{\partial X_i}\frac{\partial}{\partial \xi} + \frac{\partial \eta}{\partial X_i}\frac{\partial}{\partial \eta} + \frac{\partial \zeta}{\partial X_i}\frac{\partial}{\partial \zeta} \tag{3}$$

The procedure of the transformation of the governing equations has been described in detail by the author's other report [14]. The governing equations are discretized by finite differential method with non-staggered computational grid. The QUICK(quadratic interpolation for convective kinematics) approximation of Leonard [15] is used for discretizing convective transport term and the other terms are discretized by central-difference scheme. In numerical solution, implicit method is adopted and successive over relaxation method is utilized as a solution of the algebraic equations.

2.3 Numerical Analysis

Judging from the symmetry of CR transition duct, we set computational domain on quarter region of the whole cross section. Adding to this, upstream entry length of 30D with circular

cross section and a downstream tangent of $30D$ with rectangular cross section were used in this calculation. Therefore, total length of transition duct became $64.5D$. Reynolds number of this calculation is equal to one of the experiment.

As for the inlet condition of the straight pipe, the value of $k = U_b \times 10^{-5}$ and $\epsilon = k^{3/2}/D$ were adopted by assuming small fluctuating velocity at the duct inlet. The consistence of the universal velocity distribution at the vicinity of the wall and also the supposition of the local equilibrium lead to the utilization of the law of the wall function as the boundary conditions for k and ϵ equations. The present turbulent model is classified as a high Reynolds number model, so that we made use of wall function method.

Figure 2 shows the arrangement of the calculation mesh over the CR transition duct. Numerical grids are located finely where the variation of physical parameters are observed. Calculation has been carried out on a numerical grid with 130 nodes in the streamwise and with 25×20 in the quarter region of total cross section.

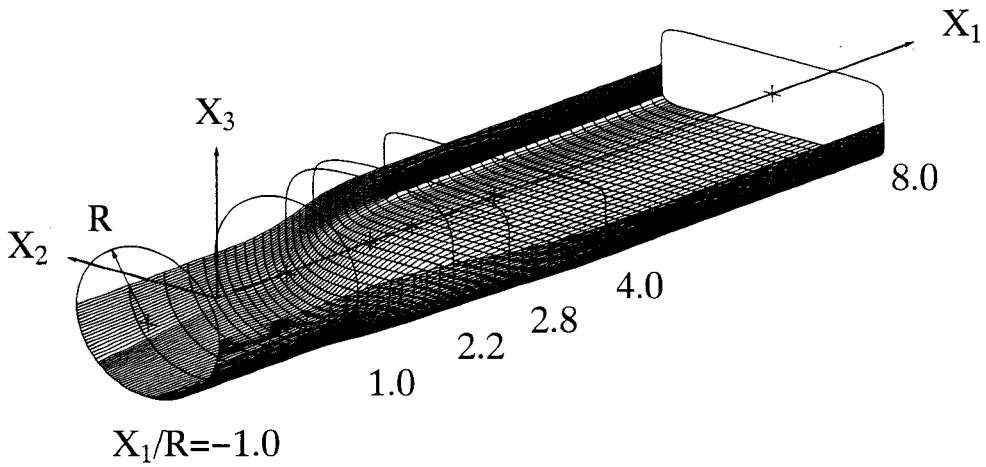

Fig.1: Subject of calculation and coordinate system

3. RESULTS AND CONSIDERATIONS

3.1 Mean Flow Results

Although the experimental results are shown in a half cross section, comparisons between both results are displayed in a quarter cross section judging from the symmetrical results of the experimental data. Streamwise mean flow are compared at X_1/R = 2.2, 2.8, 4.0 and 8.0 as shown in Fig.3. Reference coordinates applicable to theses data are shown in Fig.1. It is found from both results that streamwise velocity contours follow the cross- sectional shape at X_1/R = 2.2 and 2.8 and a distortion of contours is seen to develop in the vicinity of the sidewall at X_1/R = 4.0 and 8.0. The numerical results can reproduce these characteristic features. Moreover, it is pointed out as a discrepancy between both results that the present method is not able to predict well a distorted contours in the vicinity of the sidewall at X_1/R = 8.0. The development of distortion contour at the sidewall is very similar to the results measured

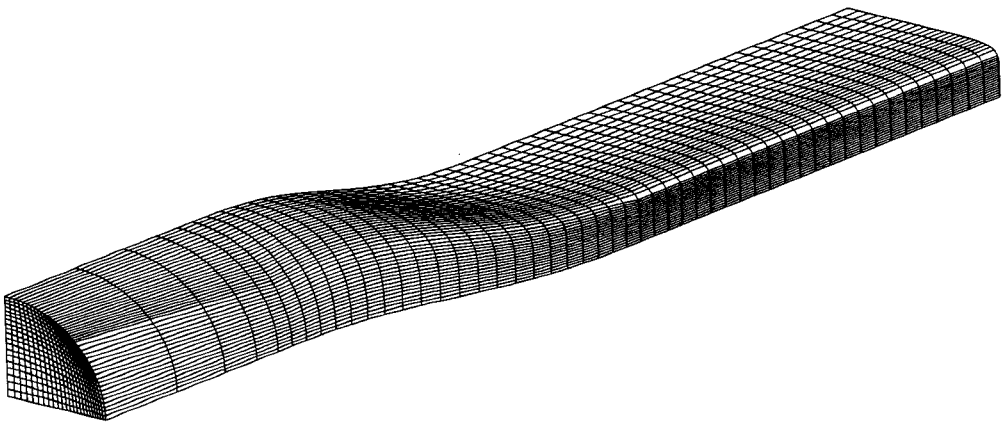

Fig.2: Arrangement of calculation mesh

by Taylor *et al.* [16] for turbulent flow through a S-shaped duct. The distortion of streamwise velocity is caused by a secondary flow which develops into a separated vortex pair along the duct sidewalls.

Figure 4 shows the comparison of secondary flow at the same cross section of streamwise velocity. The secondary flow arises as a result of lateral skewing of the near-wall flow in the vicinity of the sidewall induced by transverse pressure gradients related with wall curvature. Therefore, the secondary flow of this CR transition duct is defined as the secondary flow of the first kind. At $X_1/R = 2.2$ and 2.8, the secondary currents proceed from the center region of the duct toward sidewall. As the flow develops, the vortices have grown in lateral extent, are more circular and are centered further away from the sidewall. Between $X_1/R = 4.0$ and 8.0, the strength of the secondary flow decays gradually. These characteristic features are observed in both results. In the light of the experimental results, the present method predicts well quantitatively the secondary flow vectors. Though Lien and Leschziner [7] also presented calculated secondary vectors, the discrepancy between their results and experimental results was observed in the vicinity of the sidewall at $X_1/R = 4.0$ and 8.0.

Peripheral wall static pressure coefficient C_p, which is defined as $2(P_w - P_i)/\rho U_b^2$, distributions of both results are compared in Fig.5, where P_w and P_i denote wall static pressure and inlet static pressure, respectively. In this figure, $S/S_{ref} = 0$ and ± 1 represent the central location of upper or lower wall and it of sidewall, respectively. The normalizing S_{ref} is 1/4 of the duct circumference at a given data station. The peripheral wall static pressure is attributed to the generation of the secondary flow. At $X_1/R = 2.2$, concave curvature along the upper or lower wall($S/S_{ref} = 0.0$) induces a positive pressure gradient which results in the observed pressure peak. Conversely, convex wall curvature along the sidewalls(S/S_{ref}=± 1.0) induces negative pressure gradient resulting in the pressure minima. The radius of curvature of the wall changes sign between $X_1/R = 2.2$ and 2.8 which causes maximum and minimum pressures to occur along the side and upper or lower wall, respectively. At $X_1/R = 8.0$, there is no area change or curvature effects, and static pressure is nominally constant across the entire cross

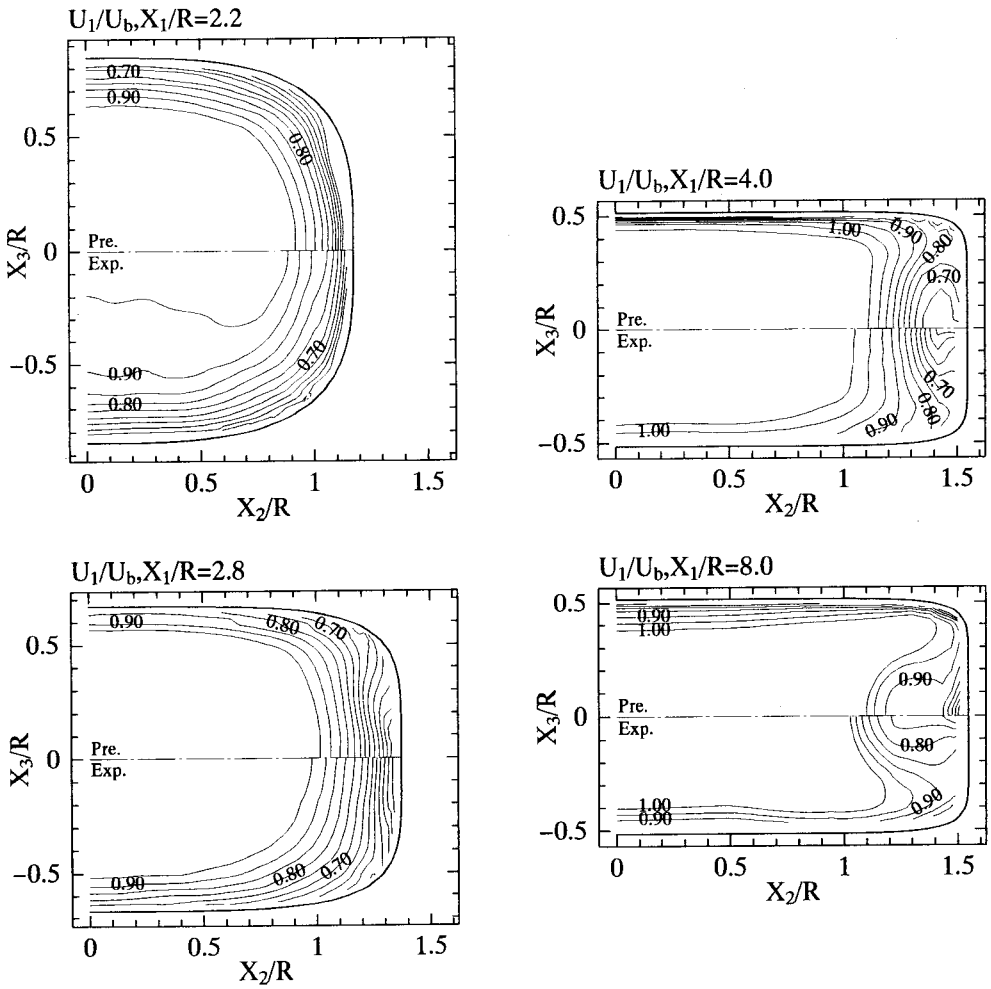

Fig.3: Comparison of streamwise velocity in CR transition duct

section. The calculated results display good agreement with these features.

3.2 Turbulence results

Figures 6, 7 and 8 show the comparison of streamwise normal stress $\overline{u_1^2}$, horizontal normal stress $\overline{u_2^2}$ and vertical normal stress $\overline{u_3^2}$, respectively. As common feature in both results, distorted contours induced by the secondary flow exist near the sidewall. These contours are distorted more clearly at $X_1/R = 8.0$ than $X_1/R = 4.0$. With regard to the experimental results of normal stress $\overline{u_3^2}$ at $X_1/R = 4.0$, $\overline{u_3^2}$ stress component exhibits two peaks symmetrically located about the $X_3/R = 0.0$ midplane which were observed at $X_1/R = 8.0$. In contrast, the appearance of these two peaks is observed not at $X_1/R = 8.0$ but at $X_1/R = 4.0$ in the calculated results. Compared with these experimental data about its value, it is found that the

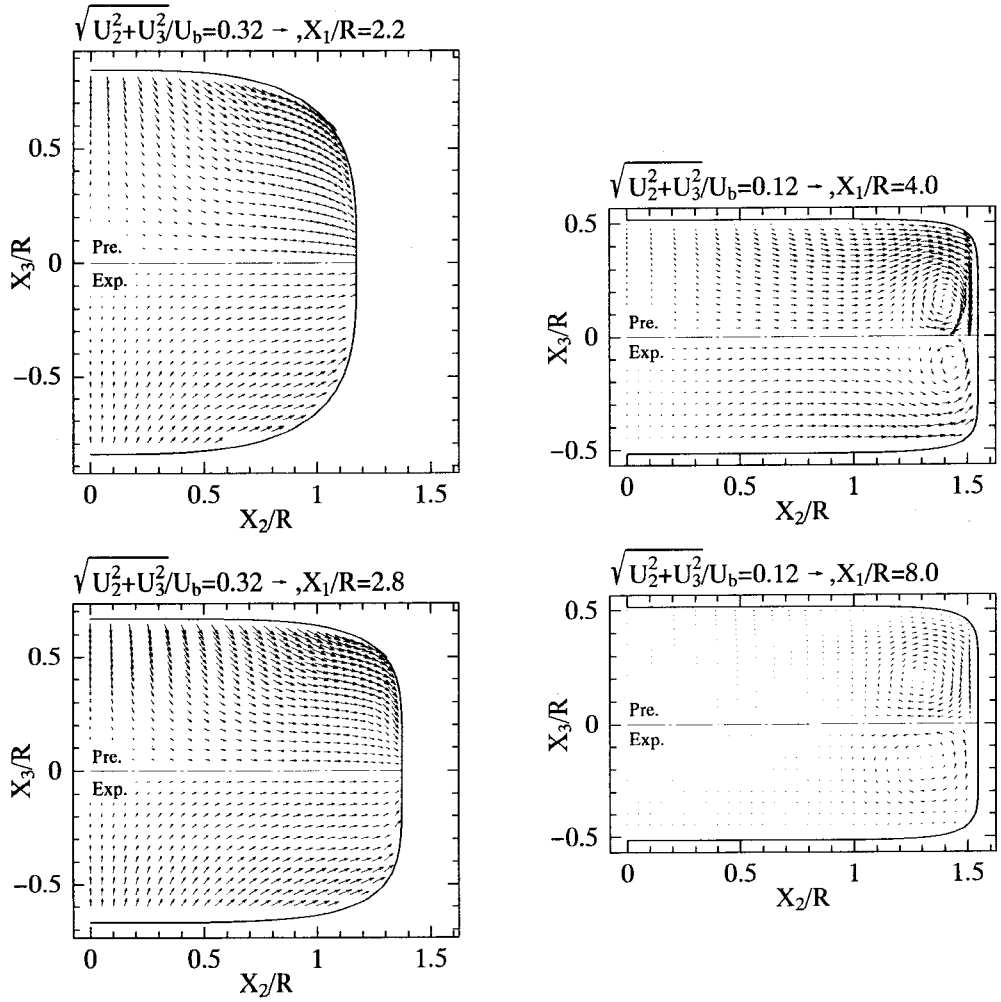

Fig.4: Comparison of secondary flow in CR transition duct

present method has a tendency to overestimate the value of these normal stresses.

The comparison of shear stress $\overline{u_1u_2}$, $\overline{u_1u_3}$ and $\overline{u_2u_3}$ are illustrated in Figs.9, 10 and 11, respectively. Negative contour levels are represented by dashed lines. As shown in Fig.9, the primary shear stress $\overline{u_1u_2}$ is observed to be positive everywhere except for small region in the vicinity of the vortex cores at $X_1/R = 4.0$ in both results. These regions of negative stress are a result of the positive mean rate-of-strain($\partial U_1/\partial X_2$) induced by distorted streamwise contours as shown in Fig.3. At downstream $X_1/R = 8.0$ of calculated results, the negative region disappears in the vicinity of sidewall as a result of secondary flow does not cause a bulging of streamwise velocity contours along the $X_3/R = 0.0$ midplane. Except for this discrepancy, the calculated results of $\overline{u_1u_2}$ are in good agreement with the experimental data.

The distributions of primary shear stress $\overline{u_1u_3}$ show the symmetrical contours with different

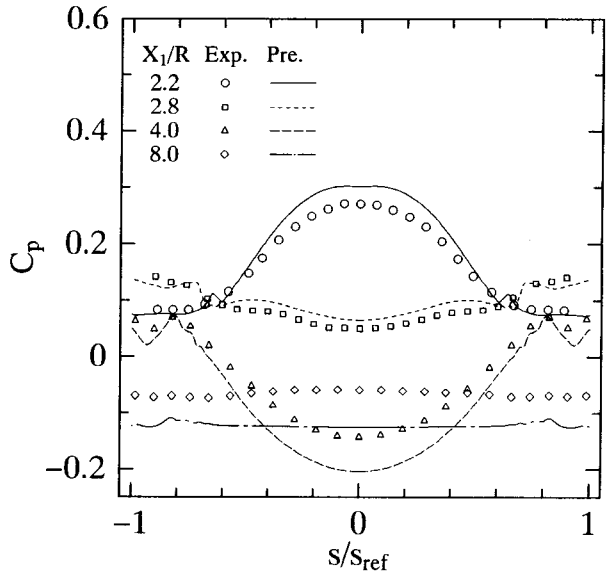

Fig.5: Comparison of peripheral wall pressure coefficient distributions

sign with respect to $X_3/R = 0.0$ midplane as displayed in Fig.10. It is found as a characteristic feature in both results that two peaks of absolute value exist near the sidewall. The present method reproduce not only qualitatively but also quantitatively the experimental distribution.

The secondary shear stress $\overline{u_2u_3}$ also shows the symmetrical distribution with different sign as well as the shear stress $\overline{u_1u_3}$. The distribution of shear stress $\overline{u_2u_3}$ are difficult to measure owing to small value compared with the other Reynolds stress. Compared the calculated results with the experiment at $X_1/R = 4.0$, it is concluded that the present method can predict its feature but has tendency to overestimate its value. At downstream $X_1/R = 8.0$, the distribution of calculated contour is similar to that of experiment.

Further insight into the structure of the turbulence can be given by examining the data through the invariant of anisotropic tensor. Invariant analysis is based on the concept of physical realizability limits of turbulence which has been used extensively to study the return to isotropy of homogeneous turbulence. Three kinds of invariant tensor which must satisfy the Caley- Hamilton theorem are defined as following equations:

$$I = b_{ij} \tag{4}$$

$$II = -\frac{1}{2}b_{ij}b_{ji} \tag{5}$$

$$III = \frac{1}{3}b_{ij}b_{jk}b_{ki} \tag{6}$$

where the anisotropic stress tensor which is first proposed by Rotta [17] is written as follows:

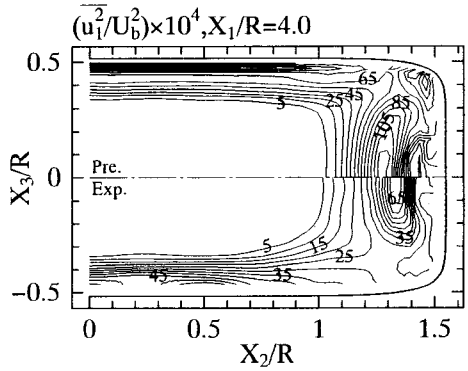

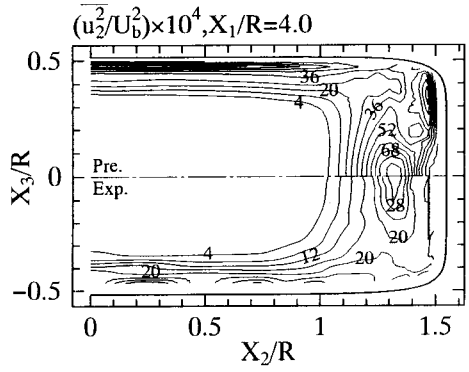

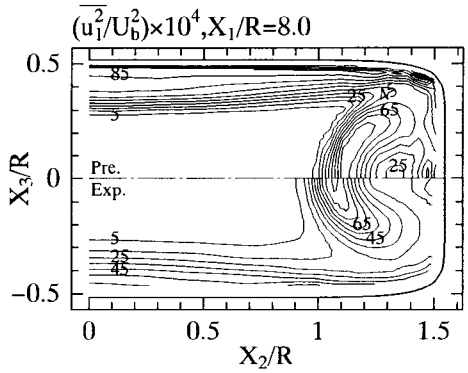

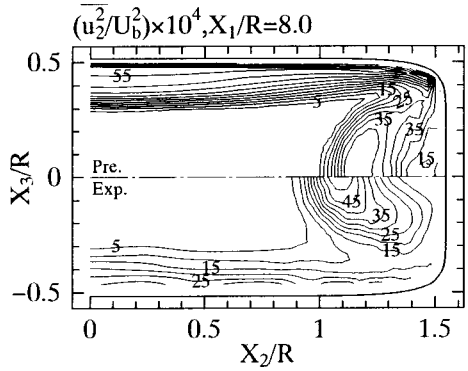

Fig.6: Comparison of normal stress $\overline{u_1^2}$

Fig.7: Comparison of normal stress $\overline{u_2^2}$

$$b_{ij} = \frac{\overline{u_i u_j} - \frac{2}{3}k\delta_{ij}}{2k} \tag{7}$$

The first invariant I is identically zero by definition of the turbulence kinetic energy. The positive value of third invariant III indicates that there is only one principle components that is large, and a negative value indicates that two principle components are large.

Figures 12 and 13 are displayed the experimental and calculated results of invariant map at $X_1/R = 4.0$, respectively. Remaining Figs.14 and 15 are the results for the experiment and calculation at $X_1/R = 8.0$, respectively. As shown in these figures, the location of each point on the invariant map relative to its position in the flow field is represented in the downward section of these figures by a vector which has its origin at $II = III = 0$ and the tip at the data point location on the invariant map. The length of vector is estimated by calculating $\sqrt{II^2 + III^2}$. Solid symbol represents the center of vortex core. At $X_1/R = 4.0$, the experimental data in invariant map exist along axisymmetric expansion line. Therefore, vectors show almost upward to the right. In the calculated results of Fig.13, scattered invariant lies between axisymmetric expansion line and axisymmetric contraction line, which phenomenon is different from the

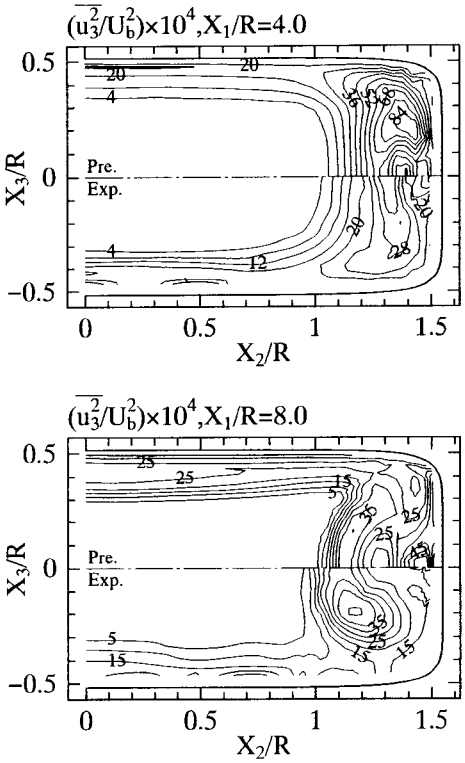

Fig.8: Comparison of normal stress $\overline{u_3^2}$

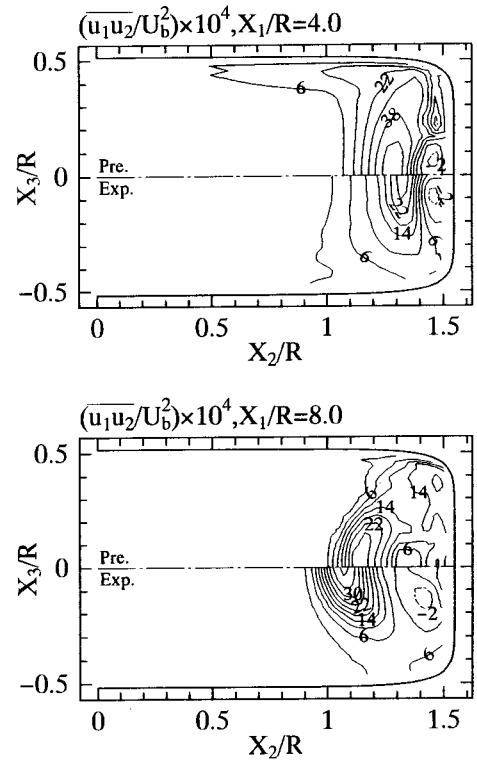

Fig.9: Comparison of shear stress $\overline{u_1u_2}$

experiment. In both results, all of the data are observed to lie within the limits of realizability and zero vector length, that means to be an isotropic condition, exists near the center of CR transition duct.

At downstream $X_1/R = 8.0$ as shown in Fig.14, the experimental distribution of invariant is similar to that of $X_1/R = 4.0$. In contrast, a lot of invariant of numerical analysis are plotted toward the axisymmetric expansion line than the axisymmetric contraction line, which is different from the numerical distribution of $X_1/R = 4.0$. In numerical analysis, vectors of upward to the left are observed near the vicinity of the sidewall of $X_3/R = 0.0$ midplane, while the experimental vectors display upward to the right. These results suggest that two principle components of Reynolds stresses are large in the numerical analysis, while one principle component is large in the experiment.

In the region of the vortex core, the turbulence becomes to be nearly isotropic by considering the vector length of the experiment. Comparing this phenomenon with the experiment, the present method also predicts its phenomenon.

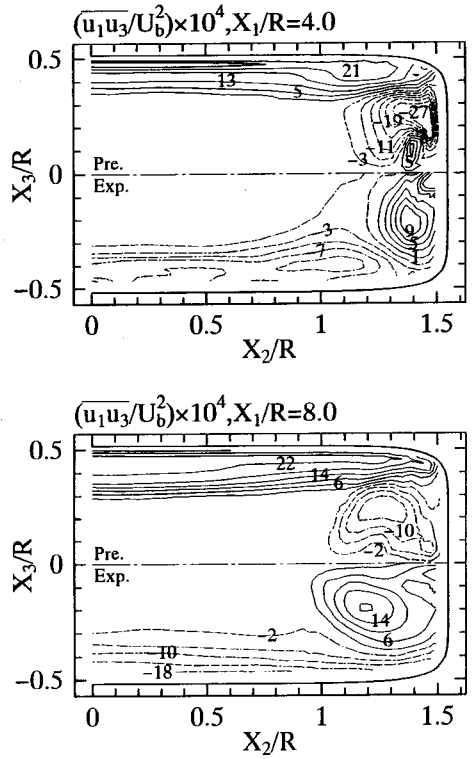

Fig.10: Comparison of shear stress $\overline{u_1 u_3}$

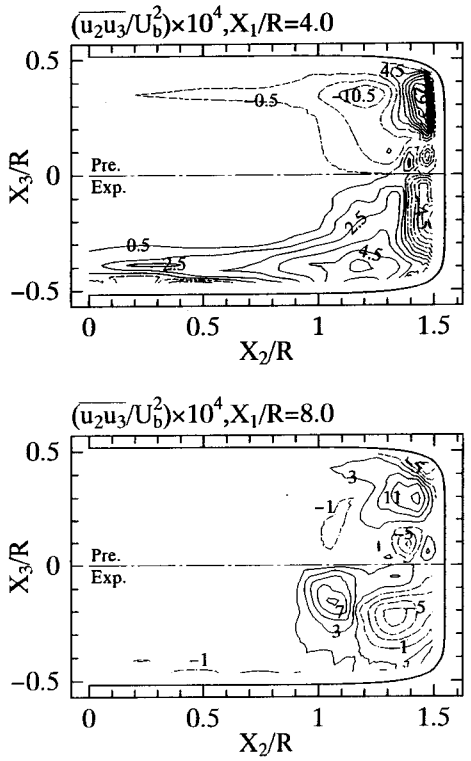

Fig.11: Comparison of shear stress $\overline{u_2 u_3}$

4. CONCLUSIONS

Numerical analysis has been carried out for developing turbulent flow in a circular-to-rectangular transition duct having the same inlet and outlet cross-section areas, an overall length-to-diameter ratio of 4.5, and aspect ratio of 3.0 at the exit plane. In order to predict precisely anisotropy turbulence of the CR transition duct, algebraic Reynolds stress model coupled with boundary-fitted coordinate system is adopted in this study. The calculated results are compared with the experimental data available to confirm the validity of the present method. The three mean velocity components, the six Reynolds stress components and the distributions of invariant were compared with the experiment. The conclusions in this research summarized as follows.

With regard to the streamwise velocity contours, the present method can reproduce the characteristic features displaying distorted contours as the flow develops except for contours of $X_1/R = 8.0$ about the midplane $X_3/R = 0.0$ in the vicinity of the duct sidewall. These distorted contours are caused by the pressure-driven secondary flow. The developments of secondary flow in the CR transition duct are predicted well by using the present method. Reasonable prediction of the secondary flow is indispensable to predict precisely the distorted

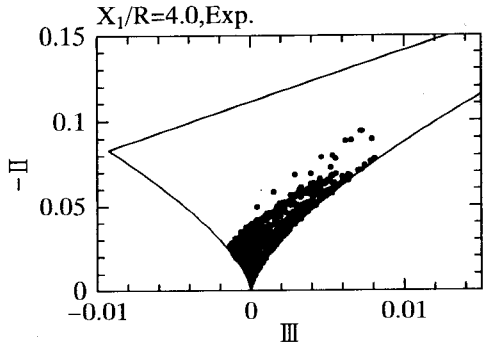

(a) Invariant map.

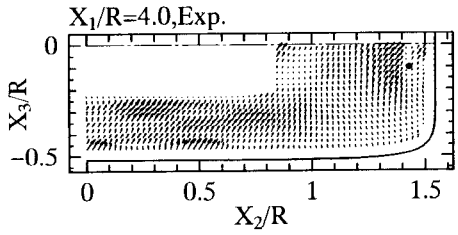

(b) Location of data points on invariant map.

Fig.12: Experimental result of invariant map plots at $X_1/R = 4.0$

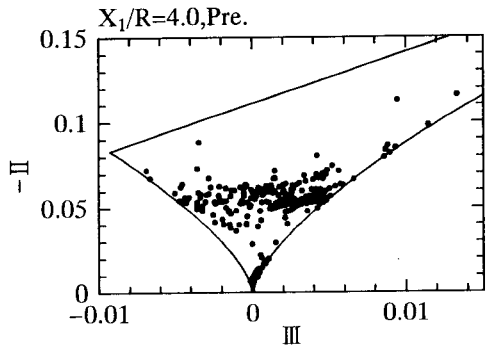

(a) Invariant map.

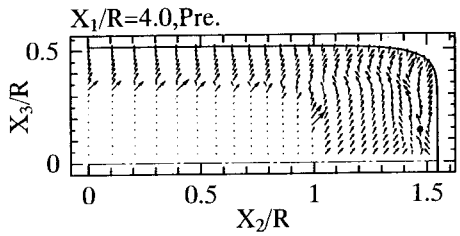

(b) Location of data points on invariant map.

Fig.13: Calculated result of invariant map plots at $X_1/R = 4.0$

contours of axial mean velocity and Reynolds stresses.

As for the normal stress of Reynolds stresses, though the present method has a tendency to overestimate its value, characteristics features are reproduced without a great discrepancy. The distributions of primary shear stresses is bound up with the gradient of streamwise velocity. The sign of shear stress $\overline{u_1 u_2}$ and $\overline{u_1 u_3}$ coincides with the sign of the primary rate of strain $\partial U_1/\partial X_2$ and $\partial U_1/\partial X_3$ deduced from contour plots of the streamwise velocity, respectively. The calculated results of shear stress are in good agreement with the experimental data.

Compared with the invariant map plots, all of the data are observed to lie within the limits of realizability in both results. But it is pointed out as a discrepancy between both results that the experimental result shows the distribution along the axisymmetric expansion line, while the calculated result are plotted widely between the axisymmetric expansion and contraction lines.

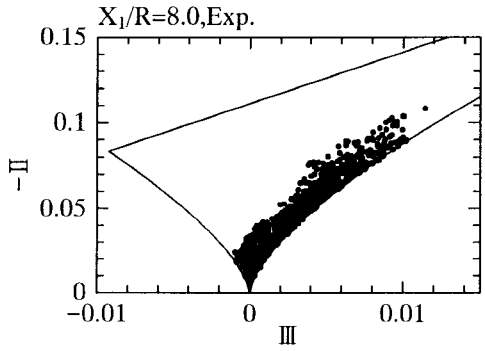

(a) Invariant map.

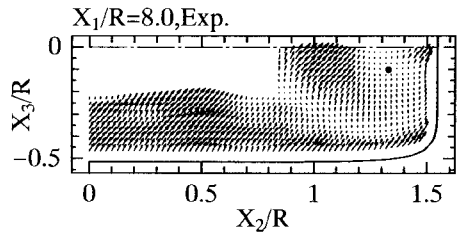

(b) Location of data points on invariant map.

Fig.14: Experimental result of invariant map plots at $X_1/R = 8.0$

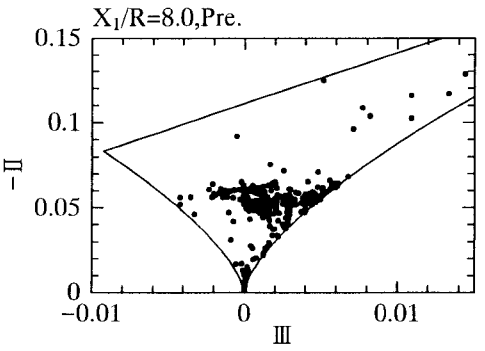

(a) Invariant map.

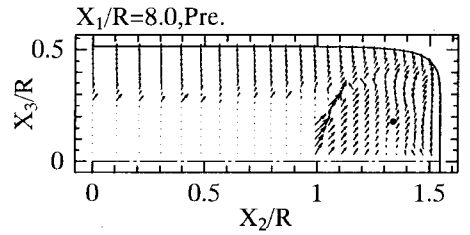

(b) Location of data points on invariant map.

Fig.15: Calculated result of invariant map plots at $X_1/R = 8.0$

Acknowledgment

The authors would like to express their appreciation to Dr. D.O.Davis (NASA Lewis Research Center) and Professor Gessner (University of Washington) for making available, in electronic form, experimental data for the CR transition duct.

REFERENCES

[1] E.Mayer (1939) Effect of transition in cross-sectional shape on the development of the velocity and pressure distribution of the turbulent flow in pipes; NACA TM903

[2] A.M.K.P.Taylor, J.H.Whitelaw and M.Yianneskis (1981) Turbulent flow in a square-to-round transition; NASA Contractor Report CR-3447

[3] W.P.Patrick and D.C.McCormick (1988) Laser velocimeter and total pressure measurements in circular-to-rectangular transition ducts; Report no.87-41, United Technology Research Center

[4] J.J.Miau, T.S.Leu, S.A.Lin and C.K.Lin (1990) Flow distortion in a circular-rectangular transition duct; AIAA Journal, vol.28 pp.1447-1456

[5] B.A.Reichert, W.R.Hingst and T.H.Okiishi (1991) An experimental comparison of

nonswirling and swirling flow in a circular- rectangular transition duct; AIAA paper 91-0342

[6] D.O.Davis and F.B.Gessner (1992) Experimental investigation of turbulent flow through a circular-rectangular transition duct; AIAA Journal, vol.30 no.2 pp.367-375

[7] F.S.Lien and M.A.Leschziner (1993) Computational modelling of 3D turbulent flow in S-diffuser and transition duct; Engineering Turbulence Modelling and Experiments 2 pp.217-227

[8] T.C.Vu and W.Shyy (1990) Navier-Stokes flow analysis for hydraulic turbine draft tubes; Trans. ASME, J. Fluids Eng., vol.12 pp.199-204

[9] D.O.Davis (1991) Experimental investigation of turbulent flow through a circular-to-rectangular transition duct; NASA TM105210

[10] W.Rodi (1976) A new algebraic relation for calculating the Reynolds stresses; Z. Angew. Math. Mech., vol.56 pp.T219-T221

[11] B.E.Launder, G.J.Reece and W.Rodi (1975) Progress in the development of a Reynolds stress turbulence closure; J. Fluid Mech., vol.68 pp.537-566

[12] F.B.Gessner and H.M.Eppich (1981) A near-wall pressure-strain model for turbulent corner flows; Proc. 3rd. Symp. Turbulent Shear Flows, vol.103 pp.445-455

[13] H.Sugiyama, M.Akiyama, M.Matsumoto, M.Hirata, and N.Ninomiya (1993) Numerical analysis of fully developed turbulent flow in a square duct with two facing roughened walls; Computational Fluid Dynamics JOURNAL, vol.2 no.3 pp.319-338

[14] H.Sugiyama, M.Akiyama, K.Yamanaka and M.Hirata (1995) Numerical analysis of turbulent structure in a rectangular duct with sand ridges; Computational Fluid Dynamics JOURNAL, vol.4. no.1 pp.59-78

[15] B.P.Leonard (1979) A stable and accurate convective modelling procedure based on quadratic upstream interpolation; Comp. Methods Appl. Mech. Eng., vol.19 pp.59-98

[16] A.M.K.P.Taylor, J.H.Whitelaw and M.Yianneskis (1984) Developing flow in S-shaped ducts, part II Circular cross section duct; NASA CR3759

[17] J.C.Rotta (1951) Statistische theorie nichthomogener turbulenz; Mitteilung-Zeitschrift für Physik, vol.129 pp.547-572